Hydrogen photogeneration using ternary $CuGaS_2$-TiO_2-Pt nanocomposites

Uriel Caudillo Flores, Anna Kubacka, Taisiia Berestok, Ting Zhang, Jordi Llorca, Jordi Arbiol, Andreu Cabot, Marcos Fernández García

Abstract

In this contribution we synthesized ternary $CuGaS_2$-TiO_2-Pt materials. The semiconductor components were surface functionalized with mercapto-alifatic acids to drive their linking and were platinized prior to or after contact between the semiconductors. The corresponding samples were utilized in the photo-production of hydrogen using methanol as a sacrificial agent. The testing under UV and visible illumination conditions together with the calculation of the true quantum efficiency of the process demonstrate the outstanding performance of these ternary materials under sunlight operation. Optimum activity was achieved for samples having a 3 to 5 wt % of the chalcogenide and a selective interaction of the noble metal with the major oxide component. The physico-chemical characterization and particularly the use of photoluminescence spectroscopy showed that photo-activity is controlled by charge separation under illumination, which drives to charge location of electrons and holes in different components of the powders and the efficient use of charge carriers in the chemical reaction.

Introduction

The efficient use of solar radiation is an important challenge in the quest for a new economy based in green and renewable technologies. In this scenario, hydrogen appears as an ideal energy vector owing to its high energy density, its extensive consolidated use in the chemical industry, and its potential eco-friendly production through photocatalysis using solar light and bio-molecules [1-7].

While bare titania and titania-based oxides have some hydrogen photo-production activity [8], the incorporation of noble metal co-catalyst boosts hydrogen generation rates several orders of magnitude [1,4,9,10-18]. Among noble metals, platinum is the most studied and used co-catalyst mainly due to its highest work function which drives to a stronger electron transfer with titania, and results in the lowest energy for proton reduction [18]. Noble metal promotion of hydrogen photo-production relies in a number of physico-chemical phenomena and catalyst parameters, including particle size and shape of the noble metal, electron-acceptor properties of the metal phase itself as well as of the charge separation properties of the metal-oxide interface. All these physico-chemical properties can have direct and beneficial effects in charge handling and, in turn, can impact the charge recombination process in a photocatalytic solid [19-32].

An important weakness of titania based photocatalysts is its wide band gap, which limits light absorption to the UV range [1-4,6]. To correct this flaw, titania can be combined with a light absorption material having a band gap in the visible range of the solar spectrum. Owing to their exceptional light absorption properties, non-toxic composition and environmentally benign character, several copper chalcogenides has been used to take full advantage of solar energy [33]. Specifically some copper chalcogenides have been used for solar light driven photo-production of hydrogen, rendering acceptable rates when promoted with Pt and other noble metals [34,35]. The combination of copper chalcogenides with titania-based materials incorporating a noble metal co-catalyst seems thus a promising composite system for achieving maximum profit from solar photons. However, to maximize activity, such a complex system, titania – copper chalcogenide – noble metal, needs to be obtained by properly assembling the three components.

Here, we study the photo-catalytic properties toward hydrogen photo-production of a titania-based system promoted by both $CuGaS_2$ (CGS) and Pt. We test the photo-production of

hydrogen using methanol as a sacrificial agent [4-6] and considering different amounts of CGS. We analyze the Pt contact with the different semiconductor phases and demonstrate that the optimum activity is achieved when Pt is preferentially in contact with the oxide semiconductor. We further present a detailed study of the UV and visible contributions to the hydrogen photogeneration, in order to understand whether a potential activity enhancement under sunlight excitation can be grounded in the properties of the titania support, the chalcogenide or both. In this direction, we calculate the true quantum efficiency of the photo-process according to the IUPAC guidelines, requiring; i) the full analysis of the optical properties of the catalysts at the liquid reaction medium, as well as ii) the modelling of the light-matter interaction at the reactor where catalytic measurements are carried out [36]. The work shows the outstanding properties of the materials for full use of UV and visible photons of the solar light. This indicates the suitability of the Pt-promoted $CuGaS_2$-TiO_2 system for optimum profiting of solar light as the energy source for the settlement of a green and economically-viable pathway for hydrogen production using sacrificial molecules from biomass. The characterization of the materials shows that charge handling by the composite system is crucial in shaping the catalytic properties of the composite system under all illumination conditions tested.

Material and methods

Preparation and chemical composition of catalysts

Materials used as precursors, solvents and other functionalities in the synthetic procedures are described in the supporting information section.

Synthesis of CGS nanocrystals (NCs): 1 mmol of copper(II) acetylacetonate ($Cu(acac)_2$) and 1 mmol of Ga(III) acetylacetonate ($Ga(acac)_3$) together with 3.5 mmol of trioctylphosphine oxide (TOPO) were mixed with 10 mL of oleylamine (OAm) upon magnetic stirring. After

degassing at 90 °C for 60 min under vacuum, an argon atmosphere was introduced and the reaction mixture was heated to 270 °C. At 150 °C, 1.12 mmol (0.25 mL) of dodecanothiol (DDT) and 7.4 mmol (1.75 mL) of *tert*-dodecanothiol (t-DDT) were injected, which changed the color of the solution from dark blue to clear yellow. While increasing temperature, the solution color further changed to clear brown, indicating the NC nucleation, and dark-brown at 250 °C. The mixture was allowed to react at 270 °C for 30 min and afterwards the heating mantle was removed to allow the solution to cool down naturally. CGS NCs were isolated by adding 5 mL of acetone and centrifuging at 5700 rpm for 5 min. The supernatant was discarded and the precipitate was redispersed in 5 mL of hexane. Additional purification steps were performed following the same procedure. Finally, NCs were redispersed in 5 mL of hexane for later use.

11-Mercaptoundecanoic acid (MUA) ligand exchange: 1 mL of a CGS NCs solution (20 mg/mL in hexane) was mixed with 1 mL of a MUA solution (4 mmol in 10 mL of methanol) at pH 10, adjusted using tetramethylammonium hydroxide (TMAOH). The resulting bi-phase solution was shaken and sonicated for 15 min. Afterwards, the upper part was removed and 5 mL of fresh acetone was added. This step was followed by centrifugation for 5 min at 5000 rpm. The obtained precipitate was redispersed in 1 mL of methanol for later use.

Titanium dioxide (TiO_2) nanoparticles (NPs): TiO_2 NPs were prepared using a microemulsion preparation method with the help of n-heptane as organic media, Triton X-100 and hexanol as surfactant and co-surfactant, respectively. The titania reference was obtained using a water in oil microemulsion and titanium tetraisopropoxide as precursor. Water/Ti and water/surfactant molar ratios were, respectively, 110 and 18 for all samples. The resulting mixture was stirred for 24 h, centrifuged, and the separated solid precursors

rinsed with methanol and dried at 110 °C for 12 h. After drying, the solid precursors were subjected to a heating ramp (2 °C min^{-1}) up to 500 °C, maintaining this temperature for 2 h.

Platinization: Pt was deposited on the surface of CGS, TiO_2 or both CGS/TiO_2 using H_2PtCl_6 as precursor. First, the material was suspended by stirring in a deionized water solution for 30 min. After that, the proper quantity (1 wt % of Pt on metal basis) of the Pt salt was added to the solution and kept on stirring along 5 min more. The reduction was carried out using a $NaBH_4$ aqueous solution (Pt/$NaBH_4$ molar ratio 1/5). The final solid was profusely rinsed with deionized water, collected by centrifugation and dried at 80 °C.

3-Mercaptopropionic acid (MPA) functionalization: TiO_2:Pt or TiO_2 NPs (150 mg) were mixed with a H_2O solution of 1 M MPA and 0.1 M H_2SO_4. The suspension was mixed for 12 h to ensure ligands attachment. The obtained sample was labelled as MPA-TiO_2(:Pt).

Ternary nanocomposite formation: CGS-TiO_2-Pt composites were obtained by introducing MPA-TiO_2 (with or without Pt) powder (150 mg) in a methanol solution containing MUA-CGS (with or without Pt) NCs (variable quantity) and sonicating the resulting suspension for at least 30 min. Afterwards, sample was precipitated by centrifuging and washed. The deposition of Pt over a specific support or in both leads to samples called CGS-TiO_2:Pt; CGS:Pt–TiO_2 and (CGS-TiO_2):Pt. The CGS-TiO_2:Pt series was analyzed in more detail. This series has samples labelled according to the nominal amount of CGS introduced: CGS1, CGS3; CGS5 and CGS8 stand for CGS-TiO_2:Pt powders containing 1, 3, 5 and 8 wt% CGS.

Characterization of catalysts

X-ray diffraction (XRD) patterns were obtained on a Policristal X'Pert Pro PANalytical diffractometer using Ni-filtered Cu Kα radiation with a 0.02° step. Material particle sizes were estimated using the Scherrer formalism [37]. Nitrogen adsorption-desorption isotherms were measured on a Micromeritics ASAP 2010. UV–vis diffuse-reflectance spectroscopy experiments were performed on a Shimadzu UV2100 apparatus using Teflon as a reference

[38]. Photoluminescence spectra were measured at room temperature on a Fluorescence Spectrophotometer Perkin Elmer LS50B. Specimens for transmission electron microscopy (TEM) characterization were prepared by drop casting the dispersions of NPs onto a 200 mesh Cu grids with ultrathin carbon and formvar support films. TEM analyses were carried out on a ZEISS LIBRA 120, operating at 120 kV. High-resolution TEM (HRTEM) and scanning TEM (STEM) studies were carried out using a field emission gun FEI Tecnai F20 microscope at 200 kV with a point-to-point resolution of 0.19 nm. High angle annular dark-field (HAADF) STEM was combined with electron energy loss spectroscopy (EELS) in the Tecnai microscope by using a GATAN QUANTUM filter. X-ray photoelectron spectroscopy (XPS) analyses were carried out on a SPECS system equipped with an Al anode XR50 source operating at 150 W and a Phoibos 150 MCD-9 detector. The pressure in the analysis chamber was kept below 10^{-7} Pa. The area analyzed was about 2 mm × 2 mm. The pass energy of the hemispherical analyzer was set at 25 eV and the energy step was maintained at 1.0 eV. Data processing was performed with the Casa XPS program (Casa Software Ltd., UK). Binding energies were shifted according to the reference C 1s peak that was located at 284.8 eV. Chemical compositions were determined using atomic emission with inductive coupled plasma (ICP-AES) using an Optima 3300DV Perkin Elmer spectrometer.

Description of the reactor

Photocatalytic measurements at liquid medium were carried out using a batch pyrex (cutting absorption edge at ca. 290 nm) reactor as depicted in Fig. S1. The reactor contained a 3:7 v/v CH_3OH/H_2O mixture medium maintained at a constant temperature (20 ± 1 °C). The catalyst suspension (0.25–1 g L^{-1} concentration) was first degassed with an Ar stream for around 20 min. Subsequently, the Ar flow was settled down to 10 mL min^{-1} and stabilized before reaction. Ar was used as carrier to displace reaction gases from the reactor to the detection system. The solution inside a reactor was irradiated using a Hg–Xe lamp (500 W) and

dichroic filters (LOT Quantum Design) allowing exposure of the catalysis to the UV (280–400 nm) or visible (420–680 nm) wavelength range. The reaction rates for hydrogen production were evaluated at 3 h from the start of the irradiation, where a pseudo-stationary situation is reached. The hydrogen rate was analyzed using on-line mass spectrometry (Onmistart 300).

Calculation of quantum efficiency

Quantum efficiency is defined, according to the IUPAC recommendation [36], as the ratio of the number of molecules reacting by the number of photon interacting with the sample. This equation takes into account that the transfer of two electrons is required to reduce two protons and produce one H_2 molecule. The reaction rate of hydrogen production (r in equation (1)) was measured in the liquid phase reactors as detailed in the previous subsection. To determine the denominator, we obtained the solution of the radiative transfer equation (RTE) in the heterogeneous reactor [39].

Results and discussion

The catalytic output of CGS-TiO_2:Pt samples with the CGS component in the 1 to 8 wt % range is presented in Fig. 1. Catalytic results are presented using UV and visible illumination. The CGS-TiO_2:Pt series was first analyzed as, according to the band positions of the composite system, electrons produced after charge separation under illumination would flow to the titania component (and subsequently to the noble metal) while holes would be accumulated in the CGS component [41]. Fig. S4 compares the catalytic output of the best sample included in Fig. 1 with other ternary configurations where Pt is selectively deposited in one of the components or in both randomly, i.e. CGS-TiO_2:Pt; CGS:Pt–TiO_2 and (CGS-TiO_2):Pt powders. We observed that the configuration presented in Fig. 1, CGS-TiO_2:Pt, maximized activity. As mentioned, his point can be rationalized by considering the fact that at CGS-TiO_2 interfaces, electrons will be driven to the oxide component. Thus, the presence

of Pt in the oxide surface will capture such electrons efficiently, particularly with respect to the capture process taking place if (Pt was) present on the chalcogenide. So, the CGS-TiO_2:Pt configuration will improve significantly charge separation as discussed below. Note that the role of the linkers proving adequate component attachment in the CGS-TiO_2:Pt configuration is important. The absence of linker between semiconductors in the preparation stage decreases the values of the CGS5 composition by ca. 1.8 times. Finally, Fig. S4 displays results from a long run utilizing the CGS5 sample, with time on stream up to 72 h. Under all illumination conditions tested here the material displayed a fairly stable catalytic activity.

Fig. 1A demonstrates that the composite ternary system is able to display enhanced activity with respect to materials having a single semiconductor under all illumination conditions tested. This result already points out at an increased activity under sunlight illumination. To quantify this increase, we analyzed the UV and visible contributions to the quantum efficiency observable (Fig. 1B). The titania reference displayed relatively high values, above 5.5 and 3.7 for, UV and visible light, respectively. These values compare reasonably well with previous reports concerning TiO_2:Pt materials. Table 2 summarizes previous reports of true quantum efficiency for the aqueous alcohol photo-reforming process. For works using a noble metal (mostly Pt but also Pd) loading in the 0.5 to 1 wt % (similar to ours), quantum efficiency values in the 1.7–5.7% range for UV and around 1–2% for visible illumination were reported [15,42-44]. Higher quantum efficiency values were occasionally reported (see Table 2) only using samples containing higher noble metal (Pt, Ru) loading (above 2.5 wt %) [45,46]. The CGS reference also presented catalytic activity. CGS activity was much lower than titania under UV and also reasonably low with respect to titania under visible light. Note that the above described conclusions consider comparisons in quantitative terms based on the measurement of the quantum efficiency, and a very different and

erroneous picture would evolve from the measurement of the reaction rates (compare, for example, panels A and B of Fig. 1).

The quantum efficiency of ternary composite materials shows also an interesting behavior throughout the series of samples containing different amounts of CGS. The measurement of both the rate (Fig. 1A) and the optical properties of the solid-liquid solution (Fig. S3) allow to unveil a strongly different behavior as a function of the illumination nature. Under UV we observed an initial decay from the titania reference but a subsequent recovery of the quantum efficiency value was noticed. The CGS5 sample displayed a relatively close value (equal within experimental error) to the titania reference. Larger concentrations of CGS in the ternary composite system were detrimental to activity (Fig. 1B). As noted, a different behavior is presented under visible illumination. The already relatively good value presented by the titania reference is increased by more than 50% for the CGS3 and CGS5 samples. With the quantum efficiency measured under UV and visible illumination we calculated the precise value for a AM1.5 solar standard, obtaining 6.5 ± 0.9 for CGS3 and 5.9 ± 0.8 for CGS5. As summarized in Table 2, the maximum values reported for noble metal-promoted (i.e. including Pt, Pd, Au or Ru) titania samples are well below 3.5% [15,17,42-46]. So, the addition of small quantities of CGS (equal or below 5 wt %) to a platinized titania sample is able to boost significantly the quantum efficiency under sunlight. To our knowledge, the CGS3 and CGS5 samples provide the highest value reported up to date for the exploitation of sunlight. This comparison also includes the use of other supports more prone to facilitate the utilization of the visible contribution of sunlight such as carbon nitride or graphene supported samples promoted with noble metals do not render quantum efficiency values above 2% [47-49].

To interpret their activity of the materials we thoroughly characterized them. Fig. 2 shows a representative TEM micrograph of the CGS NCs and their corresponding XRD, UV–vis,

photoluminescence (PL) and FTIR spectra. TEM analysis showed the average size of the NP to be ca. 20 ± 10 nm. As displayed by XRD analysis, CGS NCs crystallized in the wurtzite phase (PDF 001-1280; space group $P4_132$). EDX analysis showed the composition to match that of stoichiometric CGS with a 1:1 Cu:Ga ratio. UV–vis spectroscopy provided evidence that CGS NCs had a direct band gap at 2.5 eV, consistent with previous publications [33]. CGS NCs also displayed a broad PL peak characteristic of copper chalcogenide semiconductors and centered at around 2.9 eV. Finally, FTIR characterization pointed out that as-prepared CGS NCs contained significant amounts of organic ligands at their surface, as revealed by the presence of peaks at 2924 and 2830 cm^{-1} that correspond to C–H stretching (Fig. 2). This native surface organic ligand, most probably DDT according to previous reports [50] was displaced by MUA using a bi-phase, hexane-methanol, solution. FTIR spectrum of MUA-CGS displayed the characteristic absorbance peak of the carboxyl group at around 1695 cm^{-1}, confirming the replacement of DDT by MUA moieties.

Chemical analysis of CGSx samples provided a metal concentration of 0.4 mol. % for all co-catalysts, which was equal to the formal one within an error of 4.2% for all samples. Cu and Ga content were also in accordance with the intended weight percentage within an error of 5.6%. Fig. 3 displays the XRD pattern and the UV–vis spectrum of CGS-TiO_2:Pt powders (the CGSx samples) and TiO_2 reference. TiO_2 NPs displayed an anatase crystal phase (PDF 21-1272; space group $I4_1/amd$) and a primary particle size of ca. 12 nm as obtained from the fitting of the XRD pattern. The UV–vis spectra showed the decay characteristic of the oxide semiconductor, with a direct band gap of 3.34 eV [51]. The BET surface area of TiO_2 dried powder, calculated from nitrogen adsorption-desorption isotherms was ca. 70 $m^2 g^{-1}$ (Table 1). XRD patterns of the ternary composites prepared by mixing MPA-TiO_2:Pt with different amounts of MUA-CGS were dominated by the anatase component, with the CGS contribution being only clearly visible for the composite containing an 8 wt % CGS (Fig. 3a).

Similarly, only for the composite containing the largest amount of CGS, CGS8, a significant contribution to the UV–vis spectrum was observed (Fig. 3b). As expected, the primary particle sizes and band gap values were not modified upon physically combining the two materials. Also, the position of the valence and conduction bands do not change significantly (values within experimental error although the valence band might present an uphill shift trend with CGS content of the composites) as measured by XPS (utilized together with the band gap values obtained from UV–visible spectroscopy). Moreover, as shown in Fig. S5 the absence of changes among samples in XRD and UV–visible spectra can be extended to post-reaction specimens. This provides evidence that the materials are also stable under reaction conditions.

The composite materials were further analyzed using high resolution electron microscopy. Fig. 4 shows HAADF-STEM and bright field TEM micrographs of the CGS5 composite. In Fig. 4c a HRTEM of the nanocomposite clearly displays the TiO_2 lattice fringes and small dark spots corresponding to Pt NPs on its surface. EELS composition maps clearly displayed a very homogeneous, at the NP level, distribution of TiO_2 and CGS, with no evidences for phase separation between the two main components. Chemical species at the catalyst surface were also analyzed by XPS for the CGS5 powder. Fig. 5 shows the energy regions of O 1s, Ti 2p, Ga 2p, S 2p, Cu 2p and Pt 4d. As expected, Ti, Ga and Cu were present in just on oxidation state, Ti^{4+}, Ga^{3+} and Cu^{1+}, and three contributions were fitted to the O 1s region, corresponding to lattice oxygen in TiO_2 and different oxygen-based surface species, such as adsorbed oxygen and OH^- groups. On the other hand, the Pt 4d region was resolved with three chemical states associated to Pt^{4+} (Pt $4d_{5/2}$ = 320.5 eV, 317.5 eV), Pt^{2+} (Pt $4d_{5/2}$ = 315.0 eV) and Pt^0 (Pt $4d_{5/2}$ = 312.5 eV) [52]. This may indicate a core-shell structure for the noble metal component, with an inner metallic layer and an outer oxidized layer. Such a structure has been shown to be beneficial for photo-activity [53].

Fig. 6 displays photoluminescence profiles of the samples under UV (365 nm) and visible (425 nm) illumination. The UV spectrum of the TiO_2 reference is dominated by two kinds of transitions corresponding to the annihilation of conduction band free electrons with trapped holes and valence band free holes with trapped electron. In our samples, these transitions are located, respectively, at ca. 425 and 475–550 nm [54,55]. The spectrum is clearly different to the pure chalcogenide reported here (Fig. 2) or by others [56] using UV excitation wavelengths. The catalysts show rather similar spectral shape to the anatase reference, the main component of the powders, indicating the similar recombination process(es) taking place after illumination in these two types of solids (Fig. 6A). Main changes among samples are restricted to the intensity of the photoluminescence and can be directly interpreted as a measure of the recombination of charge in the composites. A direct correlation between photoactivity (Fig. 1) and photoluminescence intensity (Fig. 6A) can be thus established under UV illumination. This indicates the critical role of charge handling among components which in turn drive catalytic behavior.

For visible light excitation, photoluminescence spectra (Fig. 6B) show typical relatively weak signals associated to defect state(s) de-excitation over a decay curve corresponding to the excitation line [57,58]. Here some differences are encountered among samples and also with respect to the anatase reference. For CGS loadings below 5%, it appears that the presence of the chalcogenide produces a strong effect decreasing intensity for the peak at 610 to a larger extent than in the one at ca. 650 nm. This may be caused by the surface location of the first, the potential role of hole related species (depleted from titania in composite samples) in the recombination for 610 nm and may other possibilities. For the CGS8 sample the peak near 610 nm shows increasing intensity with respect to other composite samples, which seems directly associated to an enhancement of the recombination process of the corresponding titania-related defect states. In any case the important point is that the chalcogenide presence

in the composite can allow to quench defect states involved in recombination of charge and presumably detrimental for activity [54,55,57,58]. The important catalytic role of defects in (nanosized) titania as charge location (and in specific cases recombination) centers is therefore confirmed by photoluminescence [2]. The quenching of the photoluminescence intensity and thus the positive effect in catalytic properties showed parallel behavior(s), indicating that under visible light the contact between components facilitates charge handling and separation taking place for charge generated in the anatase major component. In addition to this, visible light can excite the chalcogenide component which should also suffer the charge separation induced by the contact between the two semiconductors. Both effects would positively influence photo-activity.

Thus, the presence of two components in the CGS-TiO_2:Pt system has direct influence in charge separation and handling under UV and visible illumination, with direct consequences in photo-activity. After light absorption, the generated holes required for the activation of the alcohol are accumulated at the chalcogenide component and produce protons which (previous diffusion through the water surface layer present in the materials) can be recombined to generate hydrogen with the help of the noble metal component and the cooperation of light-generated electrons [6,53]. The efficient contact among components explains the high quantum efficiency achieved under UV, visible an, particularly important, under sunlight illumination conditions.

Conclusions

In this work we prepared a ternary $CuGaS_2$-TiO_2-Pt composite system by functionalization of the semiconductor components to achieve optimum interaction and further platinization. These materials contain anatase as oxide component and wurtzite as the chalcogenide one. Testing the platinization of each (selective deposition) or both components showed a strong effect on the photo-production of hydrogen. Higher catalytic performance was achieved when

the noble metal is in exclusive contact with the anatase oxide. This seems to track the expected charge carrier flow upon illumination based in the relative position of the semiconductor bands, which would facilitate the flow of electrons to the oxide (and thus the noble metal) component and holes to the chalcogenide.

Here we report the analysis of the hydrogen photo-production using methanol as sacrificial agent as a function of the chalcogenide content of the $CuGaS_2$-TiO_2:Pt component solids under UV and visible illumination conditions relevant for the use of sunlight as the energy source of the chemical process. The $CuGaS_2$-TiO_2:Pt systems show an important response for all illumination conditions as a function of the chalcogenide content. Maximum activity is achieved for materials with a 3 to 5 wt % of the chalcogenide irrespective of the illumination conditions. The measurement of the true quantum efficiency renders an outstanding value of 6.5% under sunlight illumination, not reported previously by any other material tested in similar conditions. The characterization of the catalysts showed a strong correlation between charge separation and catalytic activity. This result indicates that the efficient contact between components drives to an improved charge separation occurring after illumination, with a direct positive impact on photo-activity, rendering the outstanding functional properties owned by the $CuGaS_2$-TiO_2:Pt composite materials.

Acknowledgements

We are thankful to MICINN (Spain) for supporting the work carried out through the ENE2016-77798-C4-1-R and ENE2016-77798-C4-3-R grants and the Secretaria de Ciencia Tecnologia e Innovacion of CDMX (SECTEI, Mexico).

References

1. K. Maeda, K. DomenPhotocatalytic water splitting: recent progress and future challenges

J Phys Chem Lett, 1 (2010), pp. 2655-2661

2. A. Kubacka, M. Fernández-García, G. ColónAdvanced nanoarchitectures for solar photocatalytic applications. Chem Rev, 112 (2012), pp. 1555-1614

3. Y. Ma, X. Wang, Y. Jia, X. Chen, H. Han, C. LiTitanium dioxide-based nanomaterials for photocatalytic fuel generations. Chem Rev, 114 (2014), pp. 9987-10043

4. X. Li, J. Yu, J. Low, Y. Fang, J. Xiao, X. ChenEngineering heterogeneous semiconductors for solar water splitting. J Mater Chem A, 3 (2015), pp. 2485-2534

5. R.A. Sene, S. Sharifnia, G.R. MoradiOn the impact evaluation of various chemical treatments of support on the photocatalytic properties and hydrogen evolution of sonochemically synthesized TiO2/Clinoptilolite. Int J Hydrogen Energy, 43 (2018), pp. 695-707

6. V. Kumaravel, S. Mathew, J. Bartlett, S.C. PillaiPhotocatalytic hydrogen production using metal doped TiO2: a review of recent advances. Appl Catal B Environ, 244 (2019), pp. 1021-1064

7. L. Clarizia, D. Russo, I. Di Somma, R. Andreozzi, R. MarottaHydrogen generation through solar photocatalytic processes: a review of the configuration and the properties of effective metal based semiconductor nanomaterials. Energies, 10 (2017), p. 1624

8. Q. Hu, J. Huang, Q. Li, C. Wang, G. Li, J. Chen, *et al.*Anatase TiO2 film composed of nanorods with predominant {110} active facets as an excellent photocatalyst for water splitting. Int J Hydrogen Energy, 42 (2017), pp. 5478-5484

9. M. Tasbihi, K. Kočí, M. Edelmannová, I. Troppová, M. Reli, R. Schomaecker Pt/TiO2 photocatalysts deposited on commercial support for photocatalytic reduction of CO2. J Photochem Photobiol A Chem, 366 (2018), pp. 72-80

10. A. Patsoura, D.I. Kondarides, X.E. VerykiosPhotocatalytic degradation of organic pollutants with simultaneous production of hydrogen. Catal Today, 124 (2007), pp. 94-102

11. J.G. Highfield, M.H. Chen, P.T. Nguyen, Z. ChenMechanistic investigations of photo-driven processes over TiO2 by in-situ DRIFTS-MS: part 1. Platinization and methanol reforming. Energy Environ Sci, 2 (2009), pp. 991-1002

12. D. Wang, T. Hisatomi, T. Takata, C. Pan, M. Katayama, J. Kubota, *et al.*Core/Shell photocatalyst with spatially separated co-catalysts for efficient reduction and oxidation of water. Angew Chem Int Ed, 52 (2013), pp. 11252-11256

13. W. Ong, L. Tan, S. Chai, S. Yong, A.R. MohamedFacet-dependent photocatalytic properties of TiO2-based composites for energy conversion and environmental remediation. ChemSusChem, 7 (2014), pp. 690-719

14. Y.-J. Yuan, J.-R. Tu, Z.-J. Ye, D.-Q. Chen, B. Hu, Y.-W. Huang, *et al.*MoS2-graphene/ZnIn2S4 hierarchical microarchitectures with an electron transport bridge between light-harvesting semiconductor and cocatalyst: a highly efficient photocatalyst for solar hydrogen generation. Appl Catal B Environ, 188 (2016), pp. 13-22

15. O. Fontelles-Carceller, M.J. Muñoz-Batista, E. Rodríguez-Castellón, J.C. Conesa, M. Fernández-García, A. KubackaMeasuring and interpreting quantum efficiency for hydrogen photo-production using Pt-titania catalysts. J Catal, 347 (2017), pp. 157-169

16. C. Zhang, Y. Zhou, Y. Zhang, S. Zhao, J. Fang, X. ShengIn situ doping of Pt active sites via Sn in double-shelled TiO2 hollow nanospheres with enhanced photocatalytic H2 production efficiency. New J Chem, 41 (2017), pp. 11089-11096

17. O. Fontelles-Carceller, M.J. Muñoz-Batista, J.C. Conesa, M. Fernández-García, A. KubackaUV and visible hydrogen photo-production using Pt promoted Nb-doped TiO2 photo-catalysts: interpreting quantum efficiency. Appl Catal B Environ, 216 (2017), pp. 133-145

18. S. TrasattiWork function, electronegativity, and electrochemical behaviour of metals: III. Electrolytic hydrogen evolution in acid solutions. J Electroanal Chem Interfacial Electrochem, 39 (1972), pp. 163-184

19.J.C. Colmenares, A. Magdziarz, M.A. Aramendia, A. Marinas, J.M. Marinas, F.J. Urbano, *et al.*Influence of the strong metal support interaction effect (SMSI) of Pt/TiO2 and Pd/TiO2 systems in the photocatalytic biohydrogen production from glucose solution. Catal Commun, 16 (2011), pp. 1-6

20. Y. Li, G. Lu, S. LiPhotocatalytic hydrogen generation and decomposition of oxalic acid over platinized TiO2. Appl Catal A Gen, 214 (2001), pp. 179-185

21. Z.H.N. Al-Azri, W.-T. Chen, A. Chan, V. Jovic, T. Ina, H. Idriss, *et al.*The roles of metal co-catalysts and reaction media in photocatalytic hydrogen production: performance evaluation of M/TiO2 photocatalysts (M= Pd, Pt, Au) in different alcohol–water mixtures. J Catal, 329 (2015), pp. 355-367

22. Y.H. Li, C. Peng, S. Yang, H.F. Wang, H.G. YangCritical roles of co-catalysts for molecular hydrogen formation in photocatalysis. J Catal, 330 (2015), pp. 120-128

23. Z. Jiang, Z. Zhang, W. Shangguan, M.A. Isaacs, L.J. Durndell, C.M.A. Parlett, *et al.* Photodeposition as a facile route to tunable Pt photocatalysts for hydrogen production: on the role of methanol. Catal Sci Technol, 6 (2016), pp. 81-88

24. J. Zhu, S. Pang, T. Dittrich, Y. Gao, W. Nie, J. Cui, *et al.*Visualizing the nano cocatalyst aligned electric fields on single photocatalyst particles. Nano Lett, 17 (2017), pp. 6735-6741

25. S. Yin, T. SatoPhotocatalytic activity of platinum loaded fibrous titania prepared by solvothermal process. J Photochem Photobiol A Chem, 169 (2005), pp. 89-94

26. C.-H. Lin, J.-H. Chao, C.-H. Liu, J.-C. Chang, F.-C. WangEffect of calcination temperature on the structure of a Pt/TiO2 (B) nanofiber and its photocatalytic activity in generating H2. Langmuir, 24 (2008), pp. 9907-9915

27. J.S. Jang, S.H. Choi, H.G. Kim, J.S. LeeLocation and state of Pt in platinized CdS/TiO2 photocatalysts for hydrogen production from water under visible light. J Phys Chem C, 112 (2008), pp. 17200-17205

28. M.A. Khan, M.S. Akhtar, S.I. Woo, O.-B. YangEnhanced photoresponse under visible light in Pt ionized TiO2 nanotube for the photocatalytic splitting of water. Catal Commun, 10 (2008), pp. 1-5

29. H. Wang, Z. Wu, Y. Liu, Y. WangInfluences of various Pt dopants over surface platinized TiO2 on the photocatalytic oxidation of nitric oxide. Chemosphere, 74 (2009), pp. 773-778

30. T. Sreethawong, C. Junbua, S. ChavadejPhotocatalytic H2 production from water splitting under visible light irradiation using Eosin Y-sensitized mesoporous-assembled Pt/TiO2 nanocrystal photocatalyst. J Power Sources, 190 (2009), pp. 513-524

31. J. Liu, G. Liu, M. Li, W. Shen, Z. Liu, J. Wang, *et al.*Enhancement of photochemical hydrogen evolution over Pt-loaded hierarchical titania photonic crystal. Energy Environ Sci, 3 (2010), pp. 1503-1506

32. S. Obregón, G. ColónImproved H2 production of Pt-TiO2/g-C3N4-MnOx composites by an efficient handling of photogenerated charge pairs. Appl Catal B Environ, 144 (2014), pp. 775-782

33. C. Coughlan, M. Ibanez, O. Dobrozhan, A. Singh, A. Cabot, K.M. RyanCompound copper chalcogenide nanocrystals. Chem Rev, 117 (2017), pp. 5865-6109

34. J. Hashemi, A. Akbari, S. Huotari, M. HakalaMulti-intermediate-band character of Ti-substituted CuGaS 2: implications for photovoltaic applications. Phys Rev B, 90 (2014), p. 75154

35. X. Yu, X. An, A. Shavel, M. Ibanez, A. CabotThe effect of the Ga content on the photocatalytic hydrogen evolution of CuIn 1− x Ga x S 2 nanocrystals. J Mater Chem A, 2 (2014), pp. 12317-12322

36. S.E. Braslavsky, A.M. Braun, A.E. Cassano, A.V. Emeline, M.I. Litter, L. Palmisano, *et al.*Glossary of terms used in photocatalysis and radiation catalysis (IUPAC Recommendations 2011). Pure Appl Chem, 83 (2011), pp. 931-1014

37. P. Scherrer“Bestimmung der Größe und der inneren Struktur von Kolloidteilchen mittels Röntgenstrahlen”. Nachrichten von Der Gesellschaft Der Wissenschaften Zu Göttingen (1918), pp. 98-100

38. P. KubelkaNew contributions to the optics of intensely light-scattering materials. Part I. J Opt Soc Am, 38 (1948), pp. 448-457

39. R.L. Romero, O.M. Alfano, A.E. CassanoCylindrical photocatalytic reactors. Radiation absorption and scattering effects produced by suspended fine particles in an annular space. Ind Eng Chem Res, 36 (1997), pp. 3094-3109

40. M.L. Satuf, R.J. Brandi, A.E. Cassano, O.M. AlfanoExperimental method to evaluate the optical properties of aqueous titanium dioxide suspensions. Ind Eng Chem Res, 44 (2005), pp. 6643-6649

41. Y. Xu, M.A.A. SchoonenThe absolute energy positions of conduction and valence bands of selected semiconducting minerals. Am Mineral, 85 (2000), pp. 543-556

42. S.E. Salas, B.S. Rosales, H. de LasaQuantum yield with platinum modified TiO2 photocatalyst for hydrogen production. Appl Catal B Environ, 140 (2013), pp. 523-536

43. U. Caudillo-Flores, M.J. Muñoz-Batista, M. Fernández-García, A. KubackaBimetallic Pt-Pd co-catalyst Nb-doped TiO2 materials for H2 photo-production under UV and Visible light illumination. Appl Catal B Environ, 238 (2018), pp. 533-545

44. U. Caudillo-Flores, M.J. Muñoz-Batista, J.A. Cortés, M. Fernández-García, A. KubackaUV and visible light driven H2 photo-production using Nb-doped TiO2: comparing Pt and Pd co-catalysts. Mol Catal, 437 (2017), pp. 1-10

45. J.F. Guayaquil-Sosa, B. Serrano-Rosales, P.J. Valadés-Pelayo, H. De LasaPhotocatalytic hydrogen production using mesoporous TiO2 doped with Pt. Appl Catal B Environ, 211 (2017), pp. 337-348

46. W. Ouyang, M.J. Munoz-Batista, A. Kubacka, R. Luque, M. Fernández-GarcíaEnhancing photocatalytic performance of TiO2 in H2 evolution via Ru co-catalyst deposition. Appl Catal B Environ, 238 (2018), pp. 434-443

47. J. Liu, Y. Liu, N. Liu, Y. Han, X. Zhang, H. Huang, *et al.*Metal-free efficient photocatalyst for stable visible water splitting via a two-electron pathway. Science 80, 347 (2015), pp. 970-974

48. M.J. Muñoz-Batista, D. Rodríguez-Padrón, A.R. Puente Santiago, A. Kubacka, R. Luque, Fernández, *et al.*Sunlight-driven hydrogen production using an annular flow photoreactor and g-C3N4-based catalysts. ChemPhotoChem, 2 (2018), pp. 870-877

49. T. Cai, Y. Liu, L. Wang, W. Dong, G. ZengRecent advances in round-the-clock photocatalytic system: mechanisms, characterization techniques and applications. J Photochem Photobiol C Photochem Rev (2019)

50. C. Xia, L. Cao, W. Liu, G. Su, R. Gao, H. Qu, *et al.*One-step synthesis of near-infrared emitting and size tunable CuInS 2 semiconductor nanocrystals by adjusting kinetic variables. CrystEngComm, 16 (2014), pp. 7469-7477

51. M. Fernández-García, A. Martínez-Arias, J.C. Hanson, J.A. RodriguezNanostructured oxides in Chemistry: characterization and properties. Chem Rev, 104 (2004), pp. 4063-4104

52. C.D. Wagner, G.E. MuilenbergHandbook of X-ray photoelectron spectroscopy: a reference book of standard data for use in X-ray photoelectron spectroscopy. Perkin-Elmer (1979)

53. M. Imizcoz, A.V. PugaAssessment of photocatalytic hydrogen production from biomass or wastewaters depending on the metal Co-catalyst and its deposition method on TiO2. Catalysts, 9 (2019), p. 584

54. T. Tachikawa, T. MajimaExploring the spatial distribution and transport behavior of charge carriers in a single titania nanowire. J Am Chem Soc, 131 (2009), pp. 8485-8495

55. C.C. Mercado, Z. Seeley, A. Bandyopadhyay, Z. Bose, J.L. McHalePhotoluminescence of dense nanocrystalline titanium dioxide thin films: effect of doping and thickness and relation to gas sensing. ACS Appl Mater Interfaces, 3 (2011), pp. 2281-2288

56. S.-H. Chang, B.-C. Chiu, T.-L. Gao, S.-L. Jheng, H.-Y. TuanSelective synthesis of copper gallium sulfide (CuGaS 2) nanostructures of different sizes, crystal phases, and morphologies. CrystEngComm, 16 (2014), pp. 3323-3330

57. M.J. Muñoz-Batista, A. Kubacka, M. Fernandez-GarciaEffect of g-C3N4 loading on TiO2-based photocatalysts: UV and visible degradation of toluene. Catal Sci Technol, 4 (2014), pp. 2006-2015

58. V. Singh, I.J.C. Beltran, J.C. Ribot, P. NagpalPhotocatalysis deconstructed: design of a new selective catalyst for artificial photosynthesis. Nano Lett, 14 (2014), pp. 597-603

Table 1. Main physico-chemical properties of the solids.[a]

Sample	**Particle size/nm**	**Band gap/eV[b]**	**BET area/m^2 g^{-1}**
TiO2	11.6	3.34	67.9
CGS1	11.3	3.22	67.0
CGS3	11.3	3.23	65.9
CGS5	11.3	3.24	66.2
CGS8	11.3	3.07	64.1
CGS	17.0	2.90	25.6

[a]Average standard error: particle size 6.1%; Band gap; 2.7%; BET area 7.9%.

[b]Anatase/CGS band gap calculated as indirect/direct gap semiconductor.

Table 2. Summary of literature reports concerning quantum efficiency measurement of the hydrogen photo-production using metal/titania catalysts.

Material	Reaction System (Liquid Phase)	Alcohol: Water (v/v %)	Catalyst concentration (g/L)	QE (%)[a]			Ref.
				UV	Vis	SL	
Pt/P25	Semi-continuous	10:90	0.5	5.6	–	–	[15]
Pt/Nb–TiO_2	Semi-continuous	40:60	0.5	5.0	2.5	3.5	[17]
Pt/P25	Batch	2:98	1.0	5.7	–	–	[42]
PtPd/Nb–TiO_2	Semi-continuous	30:70	0.5	2.9	1.2	1.4	[43]
Pt/Nb–TiO_2	Semi-continuous	30:70	0.5	1.9	0.07	–	[44]
Pd/Nb–TiO_2	Semi-continuous	30:70	0.5	1.7	0.005	–	[44]
Pt doped TiO_2	Batch	2:98	1.0	22.6	–	–	[45]
Ru/TiO_2	Semi-continuous	30:70	0.5	3.0	0.6	1.1	[46]

aQuantum efficiency values measured under UV, Visible (Vis) or Sunlight-type (SL) illumination conditions.

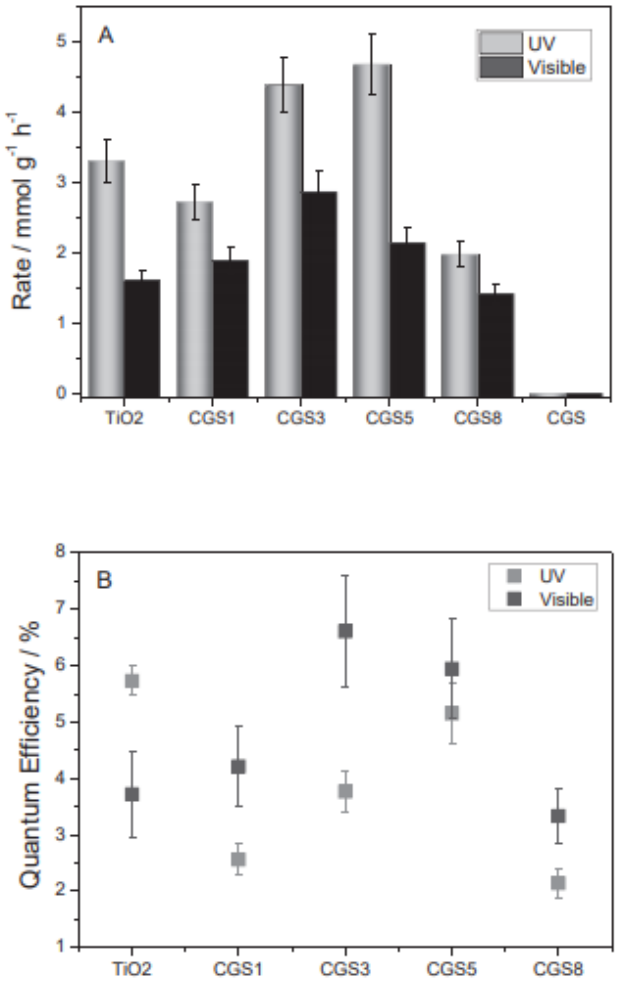

Fig. 1. Reaction rates (A) and quantum efficiency (B) of CGSx samples and TiO_2 reference.

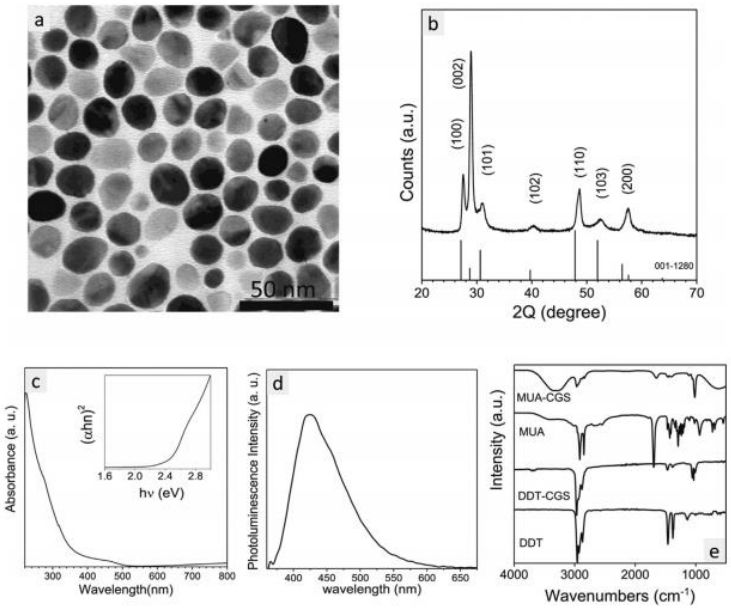

Fig. 2. CGS NCs: a) Representative TEM micrograph; b) XRD pattern including the reference for the wurtzite crystal phase (JCPDS 001–1280). c) UV–vis spectrum. d) PL spectrum. e) FTIR spectra of DDT, as produced CGS NCs (labelled as DDT-CGS), MUA and CGS NCS after ligand exchange with MUA (labelled MUA-CGS).

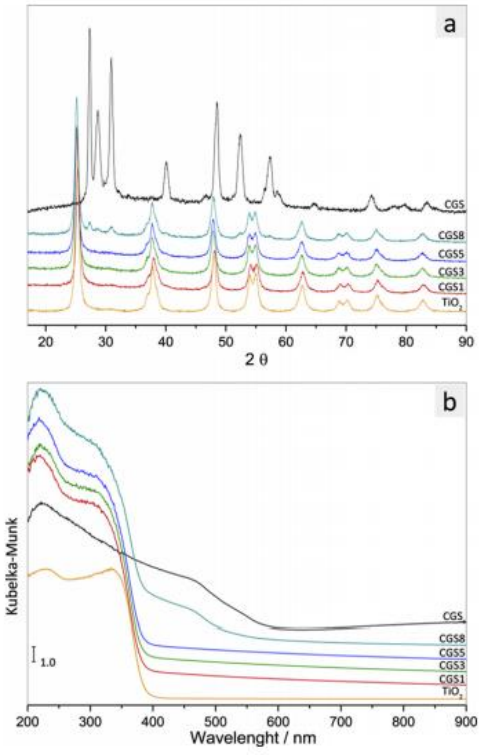

Fig. 3. XRD patterns and UV–visible spectra of the catalysts.

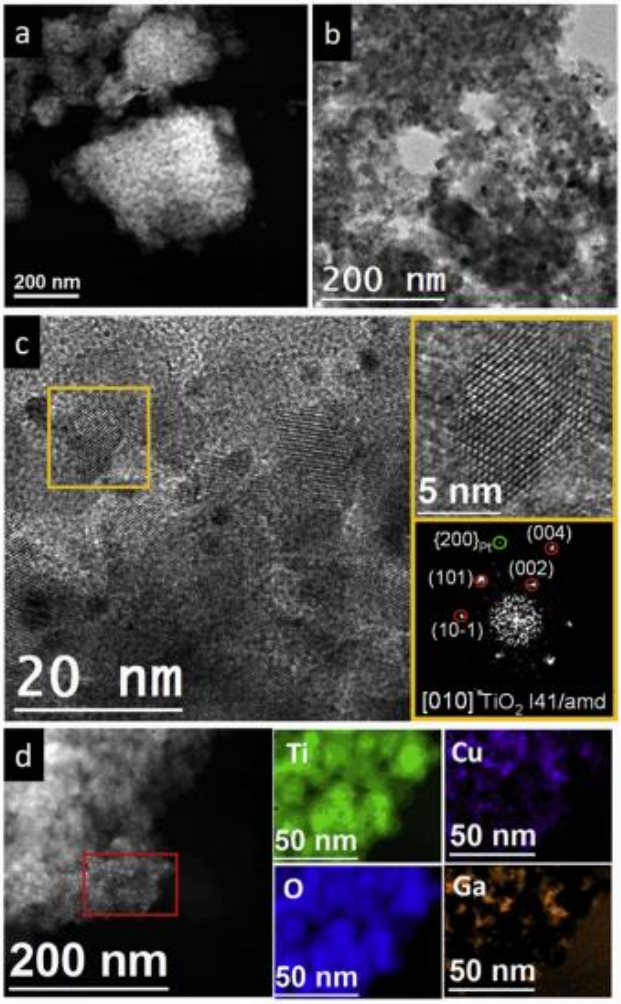

Fig. 4. Microscopy analysis of CGS5 sample: a) Representative HAADF-STEM micrograph; b) Representative HAADF-STEM micrograph; c) HRTEM micrograph, detail of the orange squared region and its corresponding power spectrum which reveals that the nanostructure has a crystal phase that is in agreement with the TiO_2 tetragonal phase (space group = $I4_1/amd$) with a = b = 3.7840 Å and c = 9.5000 Å visualized along its [010] zone axis. One of the electron diffraction spots can be matched with the (200) plane of Pt; d) EELS chemical composition maps obtained from the red squared area of the STEM micrograph. Individual Ti $L_{2,3}$-edges at 456 eV (green), O K-edges at 532 eV (blue), Cu $L_{2,3}$-edges at 931 eV (purple) and Ga $L_{2,3}$-edges at 1115 eV (orange). (For interpretation of the references to color in this figure legend, the reader is referred to the Web version of this article.)

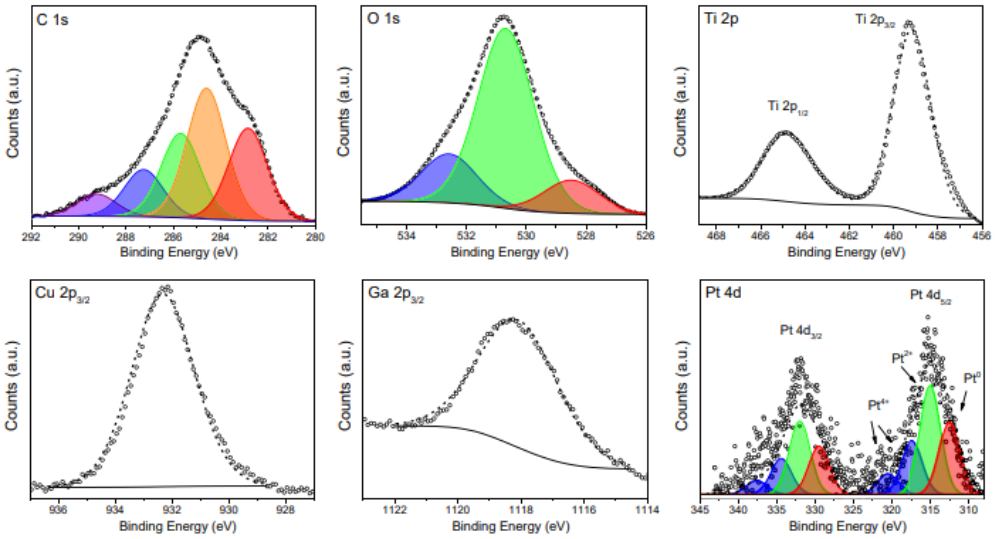

Fig. 5. C 1s, O 1s, Ti 2p, Cu $2p_{3/2}$, Ga $2p_{3/2}$ and Pt 4d regions of the XPS spectrum of the CGS5 sample.

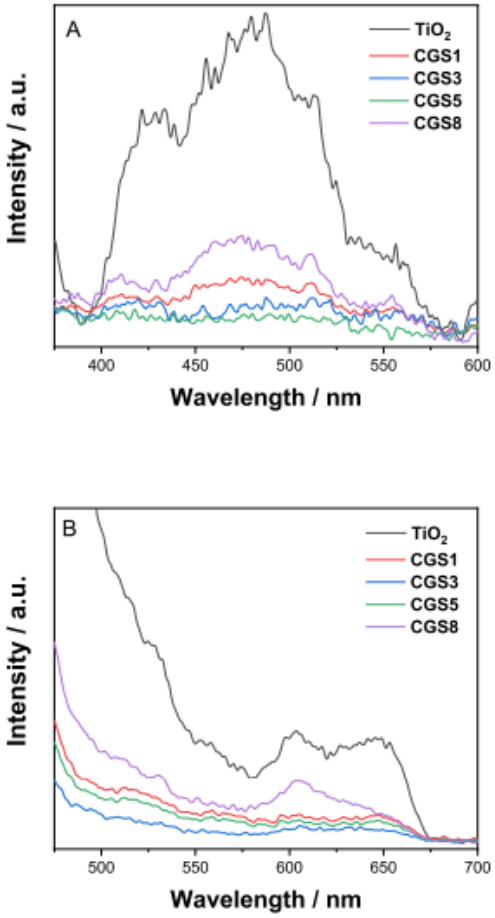

Fig. 6. Photoluminescence of CGSx samples and TiO_2 reference; (A) excitation wavelength 365 nm; (B) excitation wavelength 425 nm.